Pseudo-Random Spread Spectrum Technique Based Single-Pixel Imaging Method

Shanshan Shen ⓘ, Guohua Gu ⓘ, Tianyi Mao, Qian Chen ⓘ, Weiji He, and Jianxin Shi

Abstract—With the increasing interest in autonomous transport, machine vision and remote sensing, several three-dimensional time-of-flight (ToF) imaging technologies that can recover object's fine details have been presented. Single-pixel imaging provides an alternative to ToF photon-counting imaging with a scanned laser spot. In this work, we present a pseudo-random spread spectrum technique based single-pixel ToF imaging method, which can avoid the range ambiguity, broaden the range of signal frequencies. In addition, the Quadratic Correlation Reconstruction algorithm is applied to further increase the accuracy. With environmental light and system noise, compared to the conventional ToF single-pixel lidar we demonstrate that this approach enhances scene reconstruction quality with depth accuracy improvements of 10.5. This method may open a new gate for improved non-scanning lidar systems.

Index Terms—Pseudo-random Spread Spectrum, time-of-flight, photon counting, single-pixel imaging.

I. INTRODUCTION

THREE-dimensional (3D) Time-of-Flight (ToF) imaging techniques[1]–[3] have been applied in a number of applications, such as machine vision, remote sensing and driverless cars. A promising 3D ToF imaging modality, often called compressive sensing (CS) single-pixel lidar,utilizes an imaging scenario's compressibility to reconstruct a 3D image from an under sampled linear projection sequences. This technique images the scenario onto a series of random patterns which is loaded on a digital micro mirror device (DMD). A Geiger-mode avalanche photodiode detector (GMAPD) is used to measure the inner-product of the scenario and the random pattern [4]–[9]. During the reconstruction process, RIP (Restricted Isometry Property) is a sufficient condition. It was first proposed by Logan [10], and later developed in [11], [12]. Candes and Tao proved that if the measurement matrix was composed of random variables of independent Gaussian distribution, it can satisfy the RIP condition with the strong possibility [11]. Based on this imaging technique, optimization approaches for image restoration from projections much fewer than pixels are proposed and many reported researches have been given. Howland et al demonstrated high frame-rate video and object tracking at 32×32 pixel resolution by measuring the current signal and subtracting from it a previously acquired reference signal which the CS is well suited for [4]. Ya Nan Zhao et al presented a high efficiency single-pixel full-color imaging methods through the Hadamard basis [5]. With the limited photon counting rate, N.Radwell et al proposed a deep learning optimized imaging basis and reconstruction algorithm to improve imaging quality [6].Feng Qiang Li et al utilized total variation (TV) as the regularization function and used TwIST solver to reconstruct the image. The proposed 1-megapixel compressive ToF lidar gave spatial resolution improvements of 4 for natural scenes and the depth accuracy was analyzed by different methods [7]. Xia Lin Liu et al proposed a SP^3I technique to improve the reception efficiency of the system and the output signal-to-noise ratio (SNR) [8]. Andreas Abmann et al proposed a arrayed CS LiDAR system to approach the SNR of full frame cross-correlation based depth recovery and increase the frame rates. The reconstruction results by total variation augmented lagrangian alternating direction (TVAL3) and l_1 using gradient projection for sparse reconstruction (GPSR) are analyzed [9].Those conventional ToF single-pixel lidars often have a periodically pulsed laser source at a fixed frequency from 10 kHz to 10 MHz which limits the unambiguous range and acquisition rates. In addition, due to easily affected by noise and the contradiction between accuracy and bandwidth, such techniques often has low imaging SNR and subsequently are limited to be used indoors and in short distance imaging.

The established methodology, Pseudo-random Spread Spectrum Technique(PSST), can avoid the range ambiguity, broaden the range of signal frequencies by implementing a matched filter at the receiver end. Thus the opportunity of the entire signal fading is reduced and a strong pulse of high irradiance power by increasing the overall SNR without using excess laser

Shanshan Shen is with the School of Aeronautic Engineering, Nanjing Vocational University of Industry Technology, Nan Jing 210023, China, and also with the Jiangsu Key Laboratory of Spectral Imaging and Intelligence Sense, Nanjing University of Science and Technology, Nan Jing 210094, China (e-mail: 2020101102@niit.edu.cn).

Guohua Gu, Qian Chen, and Weiji He are with the Jiangsu Key Laboratory of Spectral Imaging and Intelligence Sense, Nanjing University of Science and Technology, Nan Jing 210094, China (e-mail: gghnjust@mail.njust.edu.cn; chenqian@njust.edu.cn; heweiji@njust.edu.cn).

Tianyi Mao is with the Jiangsu Key Laboratory of Spectral Imaging and Intelligence Sense, Nanjing University of Science and Technology, Nan Jing 210094, China, and also with the Nanjing University of Posts and Telecommunications, Nan Jing 210003, China (e-mail: maoty@njupt.edu.cn).

Jianxin Shi is with the School of Aeronautic Engineering, Nanjing Vocational University of Industry Technology, Nan Jing 210023, China (e-mail: 2018100892@niit.edu.cn).

Digital Object Identifier 10.1109/JPHOT.2022.3170941

power is formed. It has been widely used in many kinds of area, such as: wireless sensor networks [13]. Global Positioning System (GPS), and LiDAR [14]–[18]. In this paper, our system couples PSST to the ToF single-pixel lidar. A new imager called ToF single-pixel PSST (TOFSPSST) lidar is proposed. Instead of the periodical laser pulse, the laser pulse is modulated temporally by pseudo-random sequences and projected to the DMD to complete the random spatial modulation. The image sensor is used to detect and digitize the returned signal.The received signals and reference signals are cross-correlated. A linear correlated model is proposed to indicate how to multiplex the scenario points onto a single image sensor, consequently enabling us to extend CS-based reconstruction techniques such as TwIST [19] to ToF imaging. Theory model and simulation tests both prove that better SNR and depth accuracy can be achieved when using longer m-sequences. Moreover, Quadratic Correlation Reconstruction (QCR) [20], [21] is introduced to further reduce the noise effect. Finally, the edge detections are used to further show the performance of our method by computer simulation.

II. MODEL

A. Pseudo-Random Spread Spectrum Technique

The PSST based photon counting scanning imaging configuration often includes a pseudo-random sequences generator which can generate bitstream composed of 0 and 1 bits [14]–[18]. When there is a binary '1', the laser is triggered to emit laser pulse. A reference pulse correlated to the start of the output sequences is generated by the pseudo-random sequences generator and is used to arm the time-to-digital converter (TDC), which record one channel's detection time stamps of individual photons. To derive a theoretical model for the PSST, $\alpha(x,y)$ is given as the scenario's reflectivity, where (x,y) denotes two-dimensional index for transverse location on Cartesian coordinates. After the whole laser pulse is transmitted and received by GMAPD and TDC, a matched filter is applied by cross-correlating the received sequences $s(t)$ with the transmitted sequences replic $f(t)$. Thus the calculated cross-correlation signal of $(x,y)^{th}$ pixel is written as:

$$C(x,y,\tau) = \sum_{t=0}^{T} P_R \alpha(x,y) s(t) f(t+\tau)$$

$$= \begin{cases} \alpha(x,y) P_R \left[1 - \frac{T+1}{T} \frac{|\tau|}{\Delta t} \right] & |\tau| \le \Delta t \\ -\frac{1}{T} & \frac{T\Delta t}{2} \ge |\tau| > \Delta t \end{cases}. \quad (1)$$

where P_R represents the signal power, Δt represents the width of one bit. Correlation peaks can be found in (1). Often the index of the first tallest correlation peak $\tau(x,y)$ is the estimate of the photon arrival time reflected from the object with the appropriate range gate which can eliminate the back-reflection peak. Thus, the maximum-likelihood (ML) [18] estimate $\tau(x,y)_{ML}$ is written as:

$$\tau(x,y)_{ML} = \arg\max \left[C(x,y,\tau) \right] \quad (2)$$

The depth is calculated as:

$$d(x,y) = \frac{\tau(x,y) \times c}{2} \quad (3)$$

where c represents the light speed.

B. ToF Single-Pixel PSST Lidar

1) Image Process: The structure of the TOFSPSST lidar is illustrated in Fig. 1. Our method differs from the conventional single-pixel imaging method. In this paper, a pseudo-random sequences generator is used to modulate the emitted laser pulse temporally and then the modulated laser pulse is projected to the object. A DMD is used to modulate the returned laser pulse from the object spatially. Polarizing Beam Splitter (PBS) is used to separate the laser pulse retro-reflecting off the DMD from the laser pulse retro-reflecting off the object. The spatial-temporal modulated laser pulses are collected by the collection lens. The image sensor is composed of a GMAPD and a TDC. The spatial-temporal modulated light captured on the surface of the GMAPD and then digitized by TDC in temporal region at i^{th} pattern is expressed as:

$$R_i(t) = \left[\sum_{y=1}^{N} \sum_{x=1}^{N} P_R \Phi_i(x,y) \alpha(x,y) s_i(t) + B_i^{(1)}(x,y,t) \right]$$
$$+ B_i^{(2)}(t) + B^{(3)}(t) \quad (4)$$

where the random patterns loaded on the DMD is denoted as $\Phi_i(x,y)$ and the number of patterns is denoted as i. N is the number of discrete horizontal and vertical coordinates, respectively. $B_i^{(1)}(x,y,t)$ represents the environmental noise from the reflection of object. $B_i^{(2)}(t)$ represents the environmental noise from the sunlight. $B^{(3)}(t)$ represents the system noise, such as shot noise. Thus the time stamps of the TDC are correlated with the transmitted sequences replica $f(t)$. The discretely sampled signal of the ith pattern in one period T is described as follows:

$$C_i(\tau) = R_i(t) \otimes f(t)$$
$$= P_R \sum_{t=0}^{T} \left\{ \sum_{y=1}^{N} \sum_{x=1}^{N} \Phi_i(x,y) \alpha(x,y) s_i(t) + B_i^{(1)}(x,y,t) \right.$$
$$\left. + B_i^{(2)}(t) + B^{(3)}(t) \right\} f(t+\tau) \quad (5)$$

where $\otimes$ denotes the cross-correlation.

$$C_i(\tau) = P_R \sum_{t=0}^{T} \sum_{x=1}^{N} \sum_{y=1}^{N} \Phi_i(x,y) \alpha(x,y) s_i(t) f(t+\tau)$$
$$+ \underbrace{\sum_{t=0}^{T} \sum_{x=1}^{N} \sum_{y=1}^{N} B_i^{(1)}(x,y,t) f(t+\tau)}_{B_1(\tau)}$$
$$+ \underbrace{\sum_{t=0}^{T} [B_i^{(2)}(t) + B^{(3)}(t)] f(t+\tau)}_{B_2(\tau)} \quad (6)$$
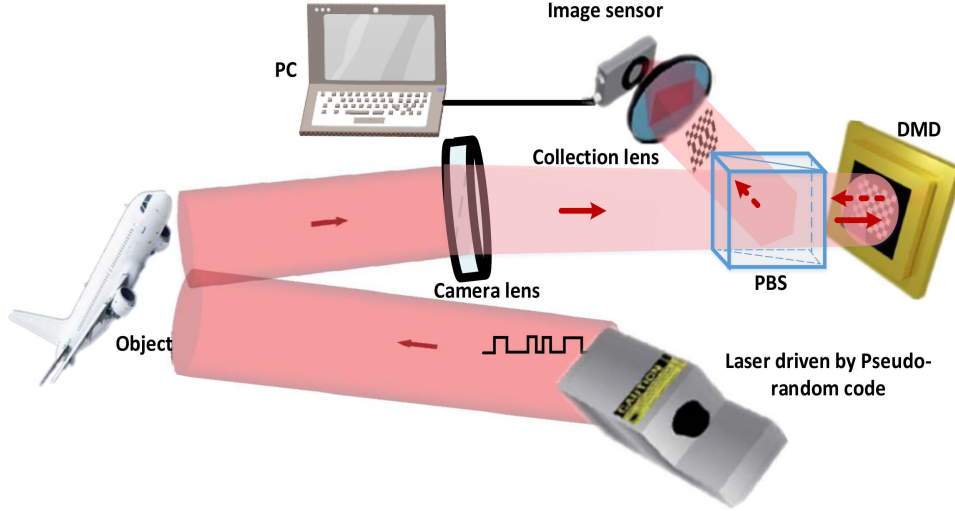
Fig. 1. The schematic diagram of our ToF single-pixel lidar based on the PPST technique.

The first item of (6) is the noiseless signal with temporal and spatial projection, the second item is the output of the environmental noise $B_1(\tau)$ from the reflection of the object, and the third item is the sunlight and system noise $B_2(\tau)$. Let $b(\tau) = B_1(\tau) + B_2(\tau)$. As shown in Fig. 1, the object reflection $\mathbf{p} \in \mathbb{R}^{Q \times 1}$ is firstly projected onto the DMD and modulated by a spatial pattern. Then, the image on the DMD plane is collected by the image sensor. We can now present the measurement model as:

$$\mathbf{C}(\tau) = \mathbf{\Phi}\mathbf{p}(\tau) + \mathbf{b}(\tau) \qquad (7)$$

with

$$p(\tau) = \begin{cases} \alpha \left[1 - \frac{T+1}{T} \frac{|\tau|}{\Delta t} \right] & |\tau| \leq \Delta t \\ -\frac{1}{T} & \frac{T\Delta t}{2} \geq |\tau| > \Delta t \end{cases}$$

where the captured intensity measurement result is $\mathbf{C} \in \mathbb{R}^{M \times 1}$, the modulation pattern produced on the DMD is $\mathbf{\Phi} \in \mathbb{R}^{M \times Q}$, the projection number is M, the random noise vector is $\mathbf{b} \in \mathbb{R}^{Q \times 1}$, and the number of pixels is $Q = N^2$.

2) Statistical Analysis: There is loss associated with the proposed imaging method caused by the optical power attenuation, scattering, the reflectivity after the interaction between the target and DMD pixels, the detector's quantum efficiency and etc. The loss problem is not considered in the proposed model. We focus on the noise robustness of the proposed imaging method. Eq. (6) shows that $C_i(\tau)$ is composed of both the signal photons C_{is} and noise photons C_{in}. One approach to studying SNR of $C_i(\tau)$ would be to find all of the statistics of these random variables in (6). In the conditions of low flux measurements, the single photon detection obeys the Poisson statistics [22]. It is assumed that noises and signals are statistically independent and the mean value is equal to the variance. Thus, the expected value of the items in (6) of the i$^{\text{th}}$ pattern in one period T is described as

follows:

$$E[C_{is}] = E\left[P_R \sum_{t=0}^{T} \sum_{x=1}^{N} \sum_{y=1}^{N} \Phi_i(x,y)\alpha(x,y)s_i(t)f(t+\tau) \right]$$

$$= TR_a M_2 \overline{\alpha} \int_{t_1}^{t_2} \frac{P_R}{hv} dt = TR_a M_2 \overline{\alpha} m_s \qquad (8)$$

$$Var[C_{in}]$$

$$= Var\left[\sum_{t=0}^{T} \sum_{x=1}^{N} \sum_{y=1}^{N} B_i^{(1)}(x,y,t)f(t+\tau) \right]$$

$$+ Var\left\{ \sum_{t=0}^{T} [B_i^{(2)}(t) + B_i^{(3)}(t)]f(t+\tau) \right\}$$

$$= E\left[\sum_{t=0}^{T} N^2 B_i^{(1)}(t)f(t+\tau) \right]$$

$$+ E\left\{ \sum_{t=0}^{T} [B_i^{(2)}(t) + B_i^{(3)}(t)]f(t+\tau) \right\}$$

$$= N^2 R_a T \int_{t_1}^{t_2} \frac{P_{B1}}{hv} dt + R_a T \int_{t_1}^{t_2} \frac{(P_{B2} + P_{B3})}{hv} dt$$

$$= N^2 R_a T m^{(1)}{}_n + R_a T m^{(2)}{}_n + R_a T m^{(3)}{}_n \qquad (9)$$

where the sampling pixel is marked by '1' in the modulation pattern, the total sampling pixels number of DMD is M_2. Let $\overline{\alpha}$ be the mean reflectivity replacing the $\alpha(x,y)$. Where E represents the mean of the variables, Var represents the variance of the variables, m_s represents the mean signal photon counts. P_{B1}, P_{B2} and P_{B3} represent the noise power of $B_i^{(1)}(x,y,t)$, $B_i^{(2)}(t)$ and $B^{(3)}(t)$ respectively. $t_2 - t_1 = \Delta t$ $m^{(1)}{}_n$, $m^{(2)}{}_n$ and $m^{(3)}{}_n$ represent the mean photon counts of the three kinds of noise respectively. The relationship between the mean photon counts and the power P_B or P_R is given in Ref [22]. h is Planck's

constant, v is the laser's optical frequency and the product hv is the photon energy. R_a is the probability of a '1' bit in the pseudo-random sequences.

The output SNR is defined as the ratio of the mean number of signal detections squared to the variance of the total number of noise and signal detections [21].The SNR model of the ith pattern in one period T is expressed as (10), shown at the bottom of this page.

It is seen that the output SNR is proportional to the sequence length T and R_a.

3) Quadratic Correlation Reconstruction: In the laser ranging system, the SNR and accuracy are affected by noise. This paper exploits a computational methodology to reduce the noise interference according to the proposed plane-to-point framework. Correlated and uncorrelated noise constitute the photoelectric noise. We can distinguish between noise and signal by the cross-correlation function. It is important to note that the signals without noise interference are generated from ensuring a rigid one-for-one correlation between object plane and modulation plane spatially and a rigid one-for-one correlation between the received time stamps and the transmitted replica temporally. But the noise is mainly generated from the system and environment. Thus the noise and signal are from separated sources, and they are uncorrelated. Direct Current component will not be generated by multiplying them together. Therefore, noise can be reduced by using quadratic correlation. Let us suppose that each column in Φ is denoted as $\varphi_z \in \mathbb{R}^{M \times 1}$ $M = 1, 2, \ldots, Q$. If the additive noise b is uncorrelated with the matrix, it can be expressed as the product of an uncorrelated random matrix $\mathbf{V}$ and the signal p,$b = \mathbf{V}p$. Then the result of the quadratic correlation of the τth dimension in (7) is shown in (11) at the bottom of this page.

According to the theory of statistics:

$$\varphi_\tau \times \varphi_j = M[\mu_\tau \mu_j + \text{cov}\,(\varphi_\tau, \varphi_j)] \tag{12}$$

$$\sum_{i=1}^{M} \varphi_{i\tau} \sum_{i=1}^{M} \varphi_{ij} = M^2 \mu_\tau \mu_j \tag{13}$$

$$\varphi_\tau \times v_j = M[\mu_\tau \mu'_j + \text{cov}\,(\varphi_\tau, v_j)] \tag{14}$$

$$\sum_{i=1}^{M} \varphi_{i\tau} \sum_{i=1}^{M} v_{ij} = M^2 \mu_\tau \mu'_j \tag{15}$$

where μ_τ μ_j and $\mu'_j$are the mean value of φ_τ φ_j and φ'_j respectively, $\text{cov}(\bullet)$ represents the covariance.

$$\Delta\,(\tau) = \sum_{j=1}^{Q} \text{cov}\,(\varphi_\tau, \varphi_j)p_j + \sum_{j=1}^{Q} \text{cov}\,(\varphi_\tau, v_j)p_j \tag{16}$$

The covariance matrix $\text{cov}(\varphi_\tau, v_j)$ is about zero. Because the spatial coherence of noise matrix and measurement matrix is low. Thus, (16) can be expressed as:

$$\boldsymbol{\Delta} = \mathbf{H}\mathbf{p} \tag{17}$$

where $\boldsymbol{\Delta} \in \mathbb{R}^{Q \times 1}$, $\mathbf{H} = \text{cov}(\boldsymbol{\Phi}, \boldsymbol{\Phi})$.

CS is a established technique that can overcome the Nyquist limit and leverage a signal's compressibility.It can reconstruct the signal with under sampled measurements lower than the Nyquist limit and thus uses optimization to recover a sparsely represented measurements. To sum up, based on the CS, if $\mathbf{p}$ is sparse enough in the basis $\boldsymbol{\Psi}$, written as $\mathbf{p} = \boldsymbol{\Psi}\mathbf{Z}$, an optimal solution of (17) can be achieved, where $\mathbf{Z}$ is the sparse coefficients. After the quadratic correlation we have $\boldsymbol{\Delta} = \mathbf{H}\boldsymbol{\Psi}\mathbf{Z} = \mathbf{A}\mathbf{Z}$, where $\mathbf{A} = \mathbf{H}\boldsymbol{\Psi}$ represents the translation matrix from the object's projection on DMD to the image sensor. The image process of TOFSPSST lidar can be modeled by interacting $\mathbf{Z}$ with a translation matrix $\mathbf{A}$. We reconstruct the image $\hat{\mathbf{Z}}$ using the following optimization:

$$\hat{\mathbf{Z}} = \arg\min_{\mathbf{Z}} \frac{1}{2} \|\boldsymbol{\Delta} - \mathbf{A}\mathbf{Z}\|^2 + \lambda\kappa(\mathbf{Z}) \tag{18}$$

where λ is the regularization parameter, $\kappa(\mathbf{Z})$ is the regularizer. In our experiment, TwIST [19] is applied to estimate $\hat{\mathbf{Z}}$ in (18). In order to balance the computational robustness and complexity, ML estimate of (3) is also introduced to optimize the reconstruction.

III. COMPUTER SIMULATIONS

To demonstrate the performance of our method, the imaging simulation experiments are performed.The pseudo-random

$$SNR = \frac{E[C_{is}]^2}{Var[C_{is} + C_{in}]} = \frac{E[C_{is}]^2}{Var[C_{is}] + Var[C_{in}]}$$

$$= \frac{(TR_a M_2 \overline{\alpha} m_s)^2}{R_a T M_2 \overline{\alpha} m_s + N^2 R_a T \overline{B_i^{(1)}(t)} + R_a T \overline{B_i^{(2)}(t)} + R_a T \overline{B^{(3)}(t)}} = \frac{TR_a (M_2 \overline{\alpha} m_s)^2}{M_2 \overline{\alpha} m_s + N^2 m^{(1)}{}_n + m^{(2)}{}_n + m^{(3)}{}_n} \tag{10}$$

$$\Delta\,(\tau) = \langle C\,(\tau), \boldsymbol{\Phi}\,(\tau)\rangle - \langle C\,(\tau)\rangle \langle \boldsymbol{\Phi}\,(\tau)\rangle = \langle \boldsymbol{\Phi}p\,(\tau) + \mathbf{V}p\,(\tau), \boldsymbol{\Phi}\,(\tau)\rangle - \langle \boldsymbol{\Phi}p\,(\tau) + \mathbf{V}p\,(\tau)\rangle \langle \boldsymbol{\Phi}\,(\tau)\rangle$$

$$= \langle \boldsymbol{\Phi}p\,(\tau), \boldsymbol{\Phi}\,(\tau)\rangle - \langle \boldsymbol{\Phi}p\,(\tau)\rangle \langle \boldsymbol{\Phi}\,(\tau)\rangle + \langle \mathbf{V}p\,(\tau), \boldsymbol{\Phi}\,(\tau)\rangle - \langle \mathbf{V}p\,(\tau)\rangle \langle \boldsymbol{\Phi}\,(\tau)\rangle$$

$$= \frac{M \sum_{j=1}^{Q}(\varphi_\tau \times \varphi_j)p_j - \sum_{i=1}^{M}\varphi_{i\tau}\sum_{i=1}^{M}\sum_{j=1}^{Q}\varphi_{ij}p_j}{M^2} + \frac{M \sum_{j=1}^{Q}(\varphi_\tau \times v_j)p_j - \sum_{i=1}^{M}\varphi_{i\tau}\sum_{i=1}^{M}\sum_{j=1}^{Q}v_{ij}p_j}{M^2} \tag{11}$$
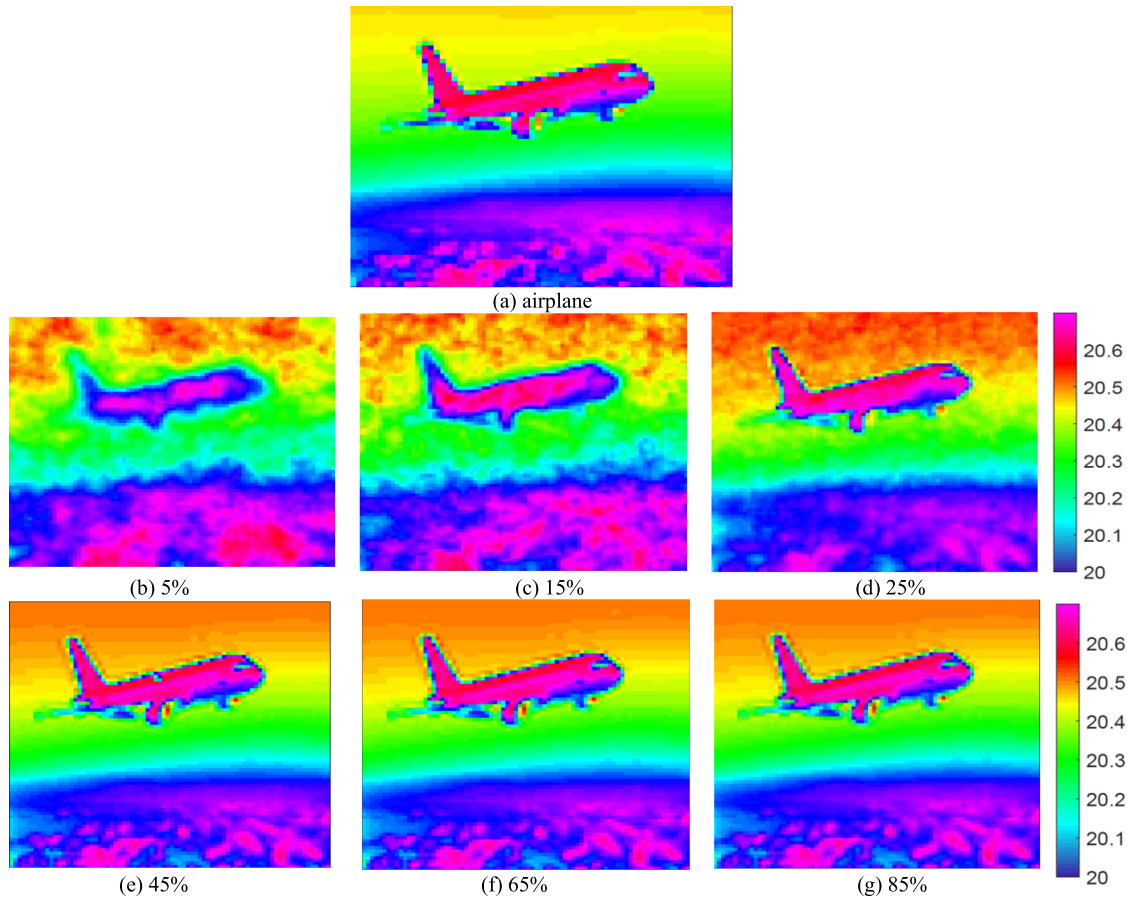
Fig. 2.   Image with different compression proportions (a) Ground truth of 'airplane'. (b)–(g) Depth maps with different compression proportions (from 5% to 85%). Colorbars show the depth information with unit of meter.
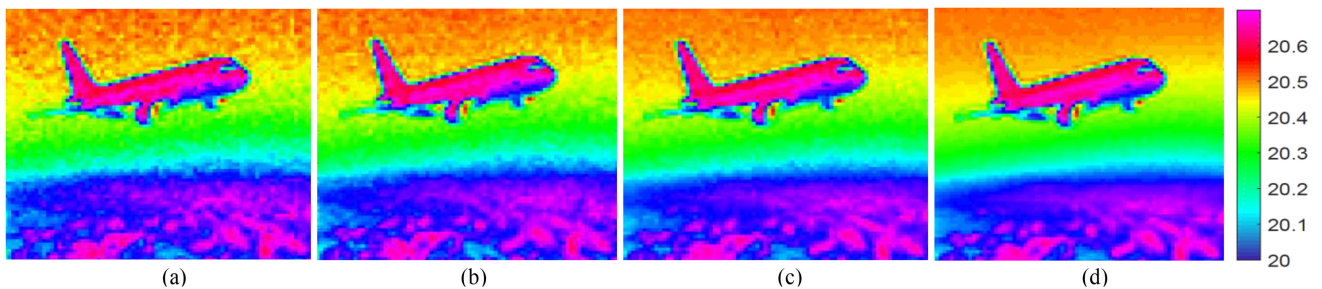

Fig. 3.   Image with different sequences (a) Depth maps by pseudo-random sequences with '1' bit of 0.1. (b) Depth maps by '1' bit of 0.3 pseudo-random sequences. (c) Depth maps by Gold sequences. (d) Depth maps by m-sequences. Colorbars show the depth information with unit of meter.

sequence pattern is in the form of a 10 GHz return-to-zero bitstream, which is then combined with a low direct current to gain-switch the vertical cavity surface emitting laser. The sequence is generated by MATLAB. The probability of a '1' bit in the pattern is determined by the random number threshold which is set to 0.1. The length of the pseudo-random sequences is 2048. The depth map of grayscale image 'airplane' is at a range of 20 to 20.8 m shown in Fig. 2(a). To detect an image, M random 64×64 Gaussian patterns sequentially placed on the DMD are generated. After obtaining the temporal and spatial projections' digitized signals, the image is reconstructed by the combination of TwIST and ML methods.

We perform the reconstruction using different compression proportions (from 5% to 85%) shown in Fig. 2(b)–(g). Compression proportion representing the compression degree is defined as $\frac{measurements}{the\ number\ of\ pixels}$. The more compression (less number of measurements) is, the faster the reconstruction is, but the worse the reconstruction quality becomes. The simulation task is completed on a PC by MATLAB. Detecting and reconstructing the image spends about 8–78 seconds relying on the compression proportions. High resolution and contrast can be achieved by 45% or less compression proportion in Fig. 2(e)–(g). But it is likely that 25% compression proportion can almost offer a acceptable result in Fig. 2(d). Mainly due to the stability
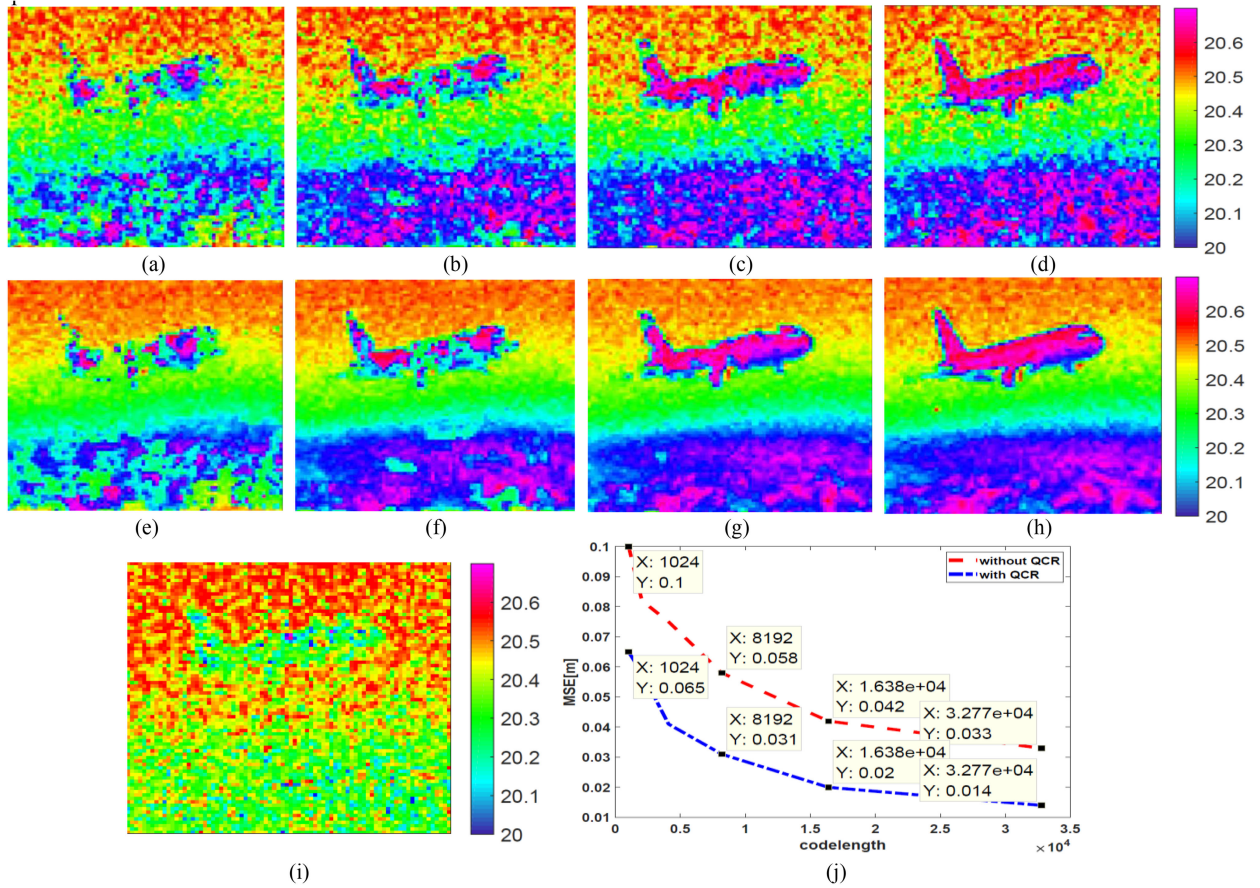
Fig. 4. Depth maps simulations without QCR by code length of (a) 2048, (b) 4096, (c) 8192, (d) 16384. Depth maps simulations with QCR by code length of (e) 2048, (f) 4096, (g) 8192, (h) 16384. (i) The depth map by conventional ToF single-pixel lidar. (j) The depth MSE with QCR (dot dashed line) and without QCR (dashed line). The depth unit is meters.
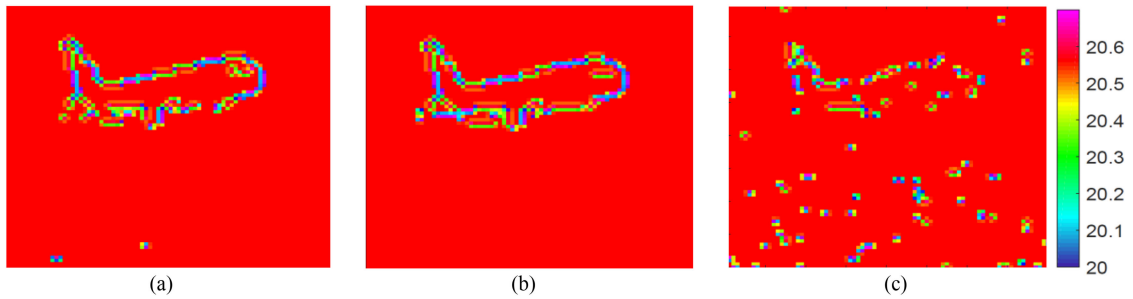

Fig. 5. Edge detection of images (a) without QCR, (b) with QCR, and (c) by a conventional ToF single-pixel lidar, respectively.

of ML, our test results are in agreement with the intensity image estimation work in Ref [7], [25]. M-sequences and Gold sequences are the most frequently used pseudo-random sequences for the uplink of CDMA systems. Gold sequences are created by the appropriate combination of m-sequences [23]. In order to compare anti-noise ability of different sequences, Poission noise is considered in our simulations. In this paper, the sum of the mean noise photon counts $m^{(1)}{}_n$, $m^{(2)}{}_n$ and $m^{(3)}{}_n$ is defined as m_n. We suppose that the mean signal photon counts defined as m_s is constant and $m_s = 5$.

TABLE I
RCONSTRUCTION STATISTICAL RECORD OF DIFFERENT METHODS

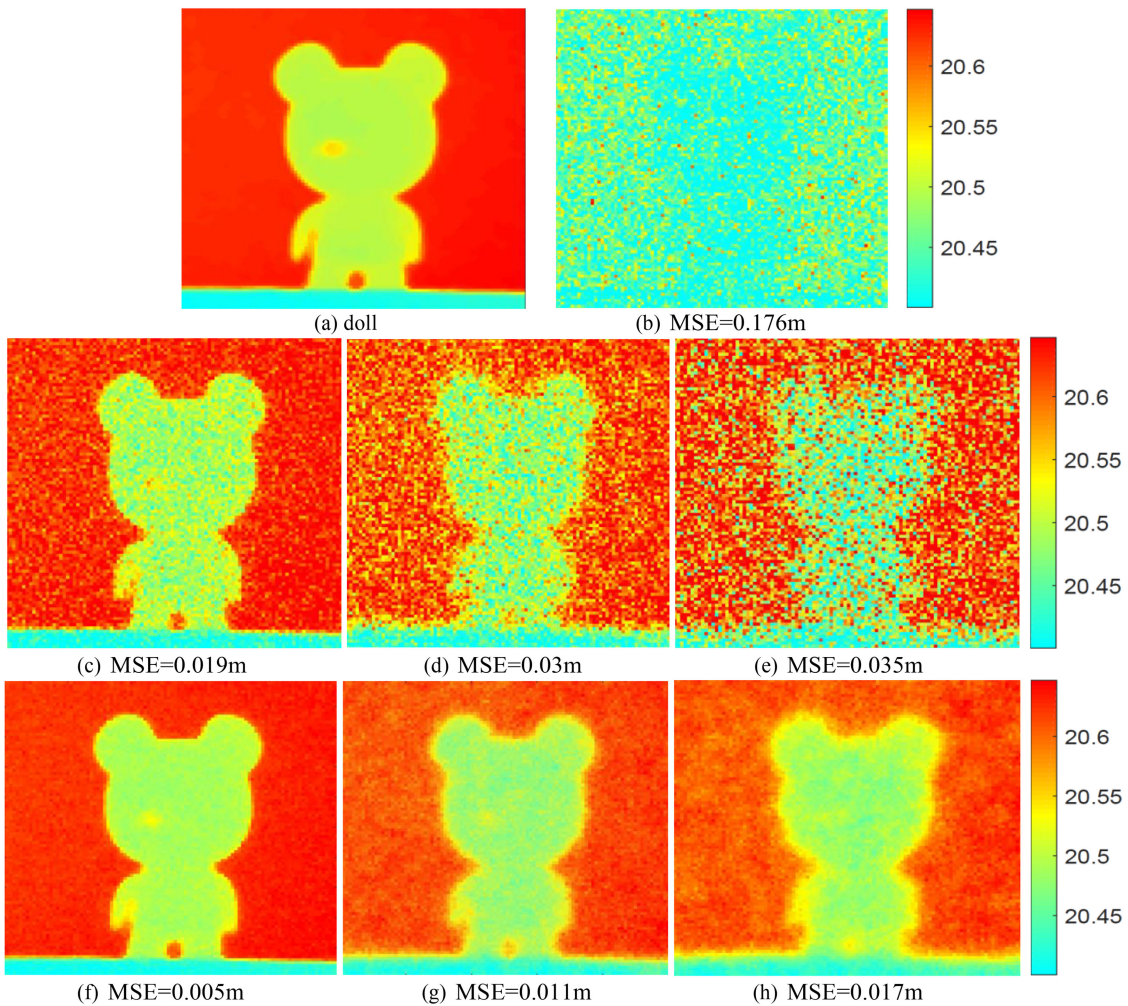| Method	MSE [cm]		Time [s]	
	$m_n = 5$	$m_n = 10$	$m_n = 5$	$m_n = 10$
TVAL3	0.033	0.011	35	57
GPSR	0.06	0.018	13	24
FISTA	0.042	0.019	16	24

Fig. 6. Depth maps reconstruction by using photon counting scanning imaging system's test image. (a) Ground truth of 'doll'. (b) The depth map by conventional ToF single-pixel lidar when $m_n = 10$. Depth maps by TOFSPSST lidar without QCR when (c) $m_n = 5$, (d) $m_n = 8$, (e) $m_n = 10$. Depth maps by TOFSPSST lidar with QCR when (f) $m_n = 5$, (g) $m_n = 8$, (h) $m_n = 10$. The depth unit is meters.
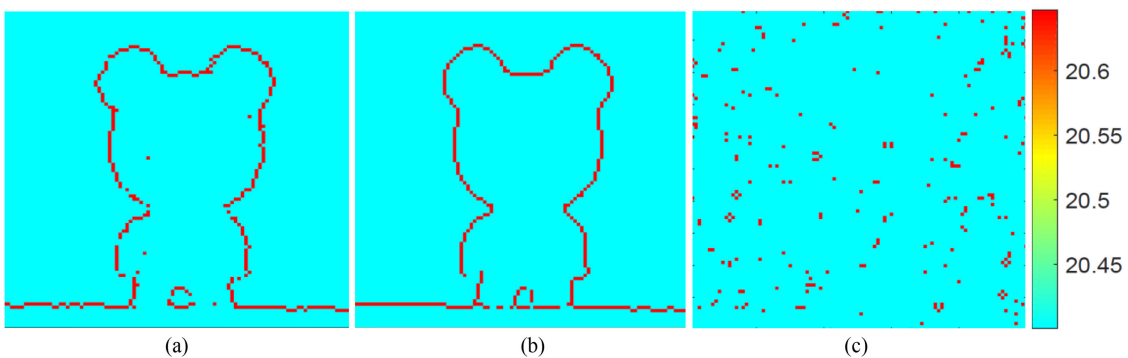

Fig. 7. Edge detection method when $m_n = 10$ (a) not using QCR, (b) using QCR, and (c) by a conventional ToF single-pixel lidar, respectively.

The interference of noise m_n is generated by a Poissian random number generator. Let $m_n = 1$ and the noise is added to the imaging process. It is observed that the reconstructions of depth maps by pseudo-random sequences with '1' bit of 0.3 shown in Fig. 3(b) is better than sequences with '1' bit of 0.1 shown in Fig. 3(a). This is consistent with the (10). Also, it is observed that the reconstructions of depth maps by m-sequences shown in Fig. 3(d) is better than Gold sequences shown in Fig. 3(c). The reason is probably that the autocorrelation performances of m-sequences are more excellent than Gold sequences.The shifted patterns of the m-sequence are also valid codes with high SNR cross-correlation [23], [24].
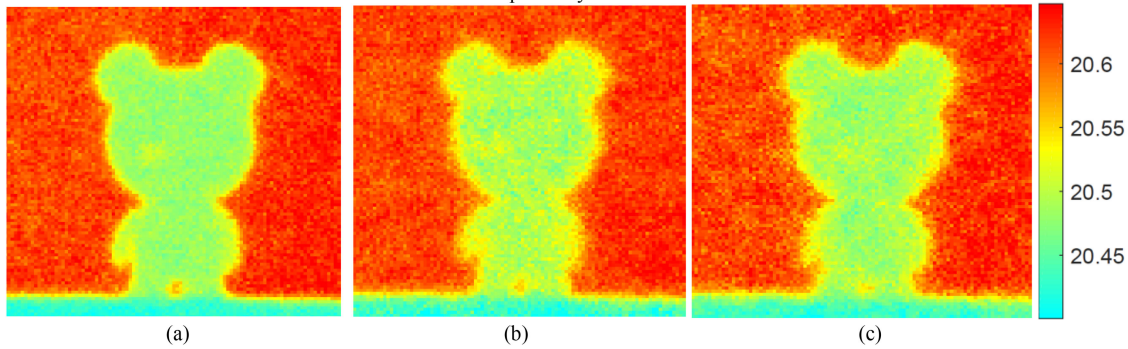
Fig. 8. Different reconstruction methods when $m_n = 10$ (a) TVAL3, (b) GPSR and (c) FISTA.

The MSE to quantify the recovery performance of the reconstructions' quality is defined as:

$$\text{MSE} = \sqrt{\frac{1}{N^2} \sum_{n=1}^{N^2} (Z_n - G_n)^2} \qquad (19)$$

Let Z_n be the reconstruction of nth pixel, G_n is defined as the ground truth data of nth pixel, and N^2 is the number of pixels.

Let $m_n = 10$, and the depth maps acquired without using QCR by m-sequences' length of 2048, 4096, 8192 and 16384 are shown in the Fig. 4(a)–(d), respectively. With the increase of the sequences' length, the image SNR enhances. This is in agreement with theoretical considerations of (10). We computed the MSE of different code length from 1024 to 32768 in Fig. 4(j). The accuracy by 32768 code length is 0.033 m. The accuracy by 1024 code length is 0.1 m. This is almost an improvement by a factor of 3. The acquisition time of the conventional ToF single-pixel lidar is the same as the proposed lidar with 16384 code length. Due to the merit of the excellent auto-correlation of m-sequences and the stability of the ML [18], under the same acquisition time, the depth map reconstructed using TOFSPSST lidar shown in Fig. 4(d) is much better than the depth map using conventional ToF single-pixel lidar shown in Fig. 4(i) in presence of environmental noise and shot noise. The results also explain the reason that most ToF single-pixel lidars fail to image when being used in long distance imaging and outdoors.

Secondly, the depth maps' MSE reconstructed using QCR shown in the Fig. 4(e)–(h) is much better than the reconstruction without QCR shown in the Fig. 4(a)–(d), which is also indicated in Fig. 4(j). We also computed that while conventional ToF single-pixel lidar gives 0.201 m of MSE depth error, the introduced QCR method gives 0.02 m. Our framework thus gives an improvement in MSE depth error by a factor of 10. Finally, we apply the Sobel operator edge detection to the image of Fig. 4(d), (h), and (i). The corresponding results are shown in Fig. 5(a)–(c) respectively. Obviously, we find that when using QCR, the reconstructed depth maps' edge detection is more robust to noise and much smoother than the other results.

At last, the real object test is achieved by using our group's photon counting scanning imaging system [26], [27]. The high accuracy depth map is acquired with the dark counts of 100c/s and per-pixel dwelling time of 1s. It represents the ground truth of the object at different distances shown in Fig. 6(a). The imaging system's depth resolution is 8ps. It is much higher than the 'airplane'. Because of this, it is seen that under the same condition the MSEs in Fig. 6(b), (e), and (h) is much smaller than the MSEs in Fig. 4(i), (d), and (h) respectively. The m-sequences length is fixed as 16384. Simulation is shown in Fig. 6. The depth map by the conventional ToF single-pixel lidar when $m_n = 10$ is shown in Fig. 6(b). Without using QCR, the results acquired by TOFSPSST lidar when $m_n = 5$ to 10 are shown in Fig. 6(c), (d), and (e) respectively. Our PPST based ToF single-pixel lidar performs better than the conventional ToF single-pixel lidar. We also computed that while conventional ToF single-pixel lidar gives 0.176 m of MSE depth error, the introduced ToF single-pixel lidar gives 0.035 m. Our imager thus gives an improvement in MSE depth error by a factor of 5. The depth maps acquired by QCR when $m_n = 5$ to 10 are shown in Fig. 6(f)–(h) respectively. Compared to the performance of the direct detection without QCR, the MSE average reduction of depth maps by the QCR is about 0.018 m at the MSE of 0.005 m to 0.017 m. The introduced method thus gives an improvement in MSE depth error by a factor of 10.5 compared to the conventional ToF single-pixel lidar. In Fig. 7, we find that when using QCR, the reconstructed depth maps' edge detection is more robust to noise and much smoother than the other results. In Fig. 8, we apply TVAL3, GPSR, FISTA to reconstruct the depth image after using the ML and QCR methods. Reconstruction results indicate that TVAL3 has the best performance.

In Table I, under different noise levels we present reconstruction statistical record of TVAL3, GPSR and FISTA to fully study the performance of those methods. The MSE results of TwIST are shown in Fig. 6. The processing time of TwIST is 20 s and 28 s according to $m_n = 5$ and $m_n = 10$ respectively. We observe from Table I that FISTA and GPSR produce almost the same quality as the TwIST with shorter amount of running time. TVAL3 trades time for accuracy and requires more adjustments of the parameter.

IV. Summary

In conclusion, we demonstrate a compact, pseudo-random sequences modulated ToF lidar that achieves transverse resolution via compressive sensing without scanning. Based on the theory

of single photon detection, the output SNR model is established. The QCR method is introduced into the simulation. The simulation test results are consistent with the theory. Such technique demonstrates the potential for long unambiguous range, strong anti-noise ability, high accuracy ToF lidar and holds feasible for other lidar data sources such as waveforms. In the future, we will develop the real ToF single pixel PSST lidar. We hope that this paper can provide the theoretical proofing of the ToF single-pixel PSST lidar and subsequently an alternative to 3D imaging techniques to improve the imaging performance for applications outdoors such as machine vision, remote sensing and autonomous vehicles.

Data Availability Statement: This manuscript has no associated data or the data will not be deposited. [Authors' comment: The datasets generated during the current study are available from the corresponding author on reasonable request.]

REFERENCES

[1] P. Rehain, Y. M. Sua, S. Y. Zhu, and I. Dickson, "Noise-tolerant single photon sensitive three-dimensional imager," *Nature Commun.*, vol. 11, no. 1, pp. 1–7, Jan. 2020.

[2] Julian Tachella and Yoann Altmann, "Real-time 3D reconstruction from single-photon lidar data using plug-and-play point cloud denoisers," *Nature Commun.*, vol. 10, no. 1, pp. 4984, Jan. 2019.

[3] J. C. Brock and S. J. Purkis, "The emerging role of lidar remote sensing in coastal research and resource management," *J. Coastal Res.*, vol. 10053, pp. 1–5, Jan. 2009.

[4] G A Howland, D J Lum, M R Ware, and J C Howell, "Photon counting compressive depth mapping," *Opt. Exp.*, vol. 21, no. 20, pp. 23822–23837, Jan. 2013.

[5] Ya Nan Zhao *et al.*, "Full-color photon-counting single-pixel imaging," *Opt. Lett.*, vol. 46, no. 19, pp. 4900–4903, Jan. 2021.

[6] N. Radwell, S. D. Johnson, M. P. Edgar, C. F. Higham, R. Murray-Smith, and M. J. Padgett, "Deep learning optimized single-pixel lidar," *Appl. Phys. Lett.*, vol. 115, no. 23, Feb. 2019, Art. no. 231101.

[7] Fengqiang Li *et al.*, "CS-ToF: High-resolution compressive time-of-flight imaging," *Opt. Exp.*, vol. 25, no. 25, pp. 31096–31110, Sep. 2017.

[8] Xialin Liu, Jianhong Shi, Lei Sun, Yonghao Li, Jianping Fan, and Guihua Zeng, "Photon-limited single-pixel imaging," *Opt. Exp.*, vol. 28, no. 6, pp. 8132–8144, Oct. 2020.

[9] Andreas Abmann, Brian Stewart, F.C. Joao, and Mota Andrew M. Wallace, "Compressive super-pixel LiDAR for high-framerate 3D depth imaging," in *Proc. IEEE Glob. Conf. Signal Inf. Process.*, 2019, pp. 1–5.

[10] B. Logan, "Properties of high-pass signals," Ph.D. dissertation, Dept. Elect. Eng., Columbia Univ., New York, NY, USA, 1965.

[11] E. Candes and T. Tao, "Near-optimal signal recovery from random projections: Universal encoding strategies?," *IEEE Trans.Inform. Theory*, vol. 52, no. 12, pp. 5406–5425, Dec. 2006.

[12] D. Donoho, "For most large underdetermined systems of linear equations the minimal ℓ1-norm solution is also the sparsest solution," *Commun. Pure Appl. Math.*, vol. 59, no. 6, pp. 797–829, Jan. 2006.

[13] P. Misra, W. Hu, M. Yang, M. Duarte, and S. Jha, "Sparsity based efficient cross-correlation techniques in sensor networks," *IEEE Trans. Mobile Comput.*, vol. 16, no. 7, pp. 2037–2050, Jul. 2017.

[14] Nils J. Krichel, Aongus McCarthy, and Gerald S. Buller, "Resolving range ambiguity in a photon counting depth imager operating at kilometer distances," *Opt. Exp.*, vol. 18, no. 9, pp. 9192–9206, Mar. 2010.

[15] Brandon Cochenour, Linda Mullen, and John Muth, "Modulated pulse laser with pseudo random coding capabilities for underwater ranging, detection, and imaging," *Appl. Opt.*, vol. 50, no. 33, pp. 6168–6178, Jun. 2011.

[16] Yu Fei Zhang and Yan He, "Three-dimensional imaging lidar system based on high speed pseudo-random modulation and photon counting," *Chin. Opt. Lett.*, vol. 14, no. 11, Jan. 2016, Art. no. 111101.

[17] Yang Yu, Bo Liu, and Zhen Chen, "Analyzing the performance of pseudo-random single photon counting ranging lidar," *Appl. Opt.*, vol. 57, no. 27, pp. 7733–7739,Jan. 2018.

[18] David M. Norman and Chester S. Gardner, "Satellite laser ranging using pseudonoise code modulated laser diodes," *Appl. Opt.*, vol. 27, no. 17, pp. 3650–3655, Sep. 1988.

[19] J. M. Bioucas-Dias and M. A. Figueiredo, "A new twIST: Two-step iterative shrinkage/thresholding algorithms for image restoration," *IEEE Trans. Image Process.*, vol. 16, no. 12, pp. 2992–3004, Dec. 2007.

[20] L Mandel and E Wolf, *Optical Coherence and Quantum Optics*. Cambridge, U.K.: Cambridge Univ. Press, 1995.

[21] Mao Tian-Yi, Chen Qian, He Wei-Ji, and Zhuang Jia-Yan, "Optical communication in turbid and turbulent atmosphere," *Acta Phys. Sin.*, vol. 65, Sep. 2016, Art. no. 08427.

[22] Philip Gatt, Steven Johnson, and Terry Nichols, "Geiger-mode avalanche photodiode ladar receiver performance characteristics and detection statistics," *Appl. Opt.*, vol. 48, no. 17, pp. 3261–3276, Jan. 2009.

[23] N. Zierler and J. Siam, "Pseudo noise sequences for engineers," *Electron. Commun. Eng. J.*, vol. 8, no. 2, pp. 5–79, Feb. 1996.

[24] Andreas F. Molisch, *Wireless Communications*, 2nd ed., Hoboken, NJ, USA: Wiley, 2011.

[25] Dai Hui dong *et al.*, "Adaptive compressed sampling based on extended wavelet trees," *Appl. Opt.*, vol. 53, no. 29, pp. 6619–6628, Feb. 2014.

[26] Shen Shanshan, Chen Qian, He Wei ji, and Gu Guo hua, "Approach for pseudo-random bit-stream multi-depth imaging," *Opt. Quantum Electron.*, vol. 52, pp. 1–9, Jan. 2020.

[27] Shen Shanshan, Chen Qian, He Wei ji, and Wang Yu Qiang, "Boundary evaluation and error correction on pseudo-random spread spectrum photon counting system," *Chin. Opt. Lett.*, vol. 15, pp. 1–9, Jun. 2017.